

Magnetohydrodynamics with Physics Informed Neural Operators

Shawn G. Rosofsky^{1,2,3} and E. A. Huerta^{1,2,4}

¹*Data Science and Learning Division, Argonne National Laboratory, Lemont, Illinois 60439, USA*

²*Department of Physics, University of Illinois at Urbana-Champaign, Urbana, Illinois 61801, USA*

³*NCSA, University of Illinois at Urbana-Champaign, Urbana, Illinois 61801, USA*

⁴*Department of Computer Science, University of Chicago, Chicago, Illinois 60637, USA*

We present the first application of physics informed neural operators, which use tensor Fourier neural operators as their backbone, to model 2D incompressible magnetohydrodynamics simulations. Our results indicate that physics informed AI can accurately model the physics of magnetohydrodynamics simulations that describe laminar flows with Reynolds numbers $Re \leq 250$. We also quantify the applicability of our AI surrogates for turbulent flows, and explore how magnetohydrodynamics simulations and AI surrogates store magnetic and kinetic energy across wavenumbers. Based on these studies, we propose a variety of approaches to create AI surrogates that provide a computationally efficient and high fidelity description of magnetohydrodynamics simulations for a broad range of Reynolds numbers. Neural operators and scientific software to produce simulation data to train, validate and test our physics informed neural operators are released with this manuscript.

I. INTRODUCTION

Turbulence emerges from laminar flow due to instabilities, has many degrees of freedom, and is commonly found in fluids with low viscosity. Its time-dependent and stochastic nature make it an ideal sandbox to explore whether AI methodologies are capable of learning and describing nonlinear phenomena that manifests from small to large scales. While the Navier-Stokes equations may be used to study flows of non-conductive fluids, flows of ionized plasmas present in astrophysical phenomena may be considered perfectly conducting. These flows may be described by magnetohydrodynamics (MHD) equations, i.e., equations with currents, magnetic fields and the Lorentz force.

Theoretical and numerical modeling of MHD turbulence is critical to understand a variety of natural phenomena, encompassing astrophysical systems [1], plasma physics [2], and geophysics [3]. Some areas of interest in which MHD turbulence plays a crucial role are binary neutron star (BNS) mergers [4], black hole accretion, and supernova explosions [1]. The inherent complexity of MHD turbulence makes the modeling of these systems extremely difficult.

One of aspects of MHD turbulence responsible for such difficulty is the MHD dynamo, which amplifies the magnetic fields by converting kinetic energy into magnetic energy, starting at the smallest scales [1, 5–7]. In some cases, the MHD dynamo can produce amplification several orders of magnitude greater than that of the original fields [1, 4]. To resolve this magnetic field amplification, one must run simulations at the smallest of scales, where the MHD dynamo is most efficient [5]. This scale is set by the Reynolds number, Re , of the flow. The higher the Re , the smaller the scale of the most efficient MHD dynamo amplification. However, astrophysical simulations in particular are at such high Reynolds numbers that it would be unfeasible to fully resolve such turbulence [7]. Therefore, we must look to alternative ways to resolve such turbulent effects. One method is to approach MHD like a large eddy simulation (LES). In LES, one ensures they possess sufficient resolution to resolve the largest eddies and employs a subgrid-scale (SGS) models to resolve turbulence at smaller scales. Some recent

works [8–19] have adopted traditional LES style SGS models for MHD simulations. Other works [20, 21] have examined the use of deep learning models as the LES model in MHD simulations. These deep learning models can use data to learn MHD turbulence properties not present in the traditional LES models, but are still in their early stages of development.

Another approach consists of accelerating scientific software used to model multi-scale and multi-physics simulations with AI surrogates. Neural operators are a very promising class of deep learning models that can accurately describe complex simulations at a fraction of the time and computational cost of traditional large scale simulations [22]. Recent studies have employed neural operators to model turbulence in hydrodynamic simulations [23–25]. In one study, the neural operators were compared to traditional LES style SGS models and were found to outperform the LES models in both accuracy and speed [25].

Physics informed neural operators (PINOs) incorporate physical and mathematical principles into the design, training and optimization of neural operators [26]. It has been reported in the literature that this approach accelerates the convergence and training of AI models, and in some cases enables zero-shot learning [27]. Several studies have illustrated the ability of PINOs to numerically solve partial differential equations (PDEs) that describe many complex problems [26, 27].

In this work we investigate the ability of PINOs to model MHD simulations. To this end, we produced 2D incompressible MHD simulations spanning a broad range of Reynolds numbers. We then trained the PINOs with these data and evaluated them on a subset of simulations not observed in training. Specifically, we compared the PINO predictions and the simulation values as well as their kinetic and magnetic energy spectra. To the best of our knowledge, this is the first study seeking to reproduce entire MHD simulations with deep learning models. As such, we focused our efforts on finding the strengths and weaknesses of this approach rather than optimizing our models as much as possible. In doing so, this work provides a foundation of AI surrogates for MHD that future researchers will improve upon.

We organize this work as follows. In Section II we introduce the incompressible MHD equations, and describe the numeri-

cal methods used to generate MHD simulation data. Then, we describe PINOs, and how we used them to solve MHD equations in Section III. Section IV details the methods we followed to create our PINOs, including generation of random initial data, model architecture, training procedure, evaluation criteria, and a description of our computational resources. We present the results in Section V. Final remarks and future directions of work are presented in Section VI.

II. SIMULATING INCOMPRESSIBLE MHD

A. Equations

The goal of this work is to reproduce the incompressible MHD equations with PINOs. The incompressible MHD equations represent an incompressible fluid in the presence of a magnetic field \mathbf{B} . These equations are given by

$$\partial_t \mathbf{u} + \mathbf{u} \cdot \nabla \mathbf{u} = -\nabla \left(p + \frac{B^2}{2} \right) / \rho_0 + \mathbf{B} \cdot \nabla \mathbf{B} + \nu \nabla^2 \mathbf{u}, \quad (1)$$

$$\partial_t \mathbf{B} + \mathbf{u} \cdot \nabla \mathbf{B} = \mathbf{B} \cdot \nabla \mathbf{u} + \eta \nabla^2 \mathbf{B}, \quad (2)$$

$$\nabla \cdot \mathbf{u} = 0, \quad (3)$$

$$\nabla \cdot \mathbf{B} = 0, \quad (4)$$

where \mathbf{u} is the velocity field, p is the pressure, B is the magnitude of the magnetic field, $\rho_0 = 1$ is the density of the fluid, ν is the kinetic viscosity, and η is the magnetic resistivity. We have two equations for evolution and two constraint equations.

To ensure the zero velocity divergence condition of Equation (3), the pressure is typically computed in such a way that this condition always holds true. This is generally done by solving a Poisson equation to calculate the pressure at each time step.

For the magnetic field divergence of Equation (4), we lack any additional free parameters to ensure that the equation holds true at all times. There are several ways to ensure that this condition holds including hyperbolic divergence cleaning [28] and constrained transport [29]. For this work, we decide to preserve the magnetic field's zero divergence condition by instead evolving the magnetic vector potential \mathbf{A} . This quantity is defined such that

$$\mathbf{B} = \nabla \times \mathbf{A}, \quad (5)$$

which ensures that the divergence of \mathbf{B} is zero to numerical precision as the divergence of a curl of a vector field is zero. By evolving magnetic vector potential \mathbf{A} instead of the magnetic field \mathbf{B} , we have a new evolution equation for the vector potential \mathbf{A} . This equation is given by

$$\partial_t \mathbf{A} + \mathbf{u} \cdot \nabla \mathbf{A} = \eta \nabla^2 \mathbf{A}. \quad (6)$$

B. Numerical Methods

To simulate the MHD equations, we employed the Dedalus code [30], an open source parallelized spectral python package that is designed to solve general PDEs. To obtain interesting results without additional computational difficulty, we elected to solve the incompressible MHD equations in 2D with periodic boundary conditions (BCs). This results in us solving a total of 3 evolution PDEs at each timestep—2 for the velocity evolution and 1 for the magnetic vector potential evolution. To visualize and more easily diagnose problems with the simulations, we include an additional PDE to evolve tracer particles denoted by s . The tracer particles had an evolution equation given by

$$\partial_t s + \mathbf{u} \cdot \nabla s = \nu \nabla^2 s. \quad (7)$$

Moreover, we employed a pressure gauge of $\int p dx^2 = 0$ for our equation. Numerically, most simulations were carried out on a unit length square grid at resolutions with a total number of grid points $N = 128^2$, with $N_x = N_y = 128$ points in the x and y directions, respectively. We also examined some higher resolution simulations with $N = 256^2$ (and $N = 512^2$) to explore how resolution may affect the results of the simulations.

As we have periodic BC, we employed a Fourier basis in each direction. To avoid aliasing error, we used a dealias factor of 3/2 for these transformations. For timestepping, we used the RK4 integration method with a constant timestep of $\Delta t = 0.001$. Simulation outputs were stored every 10 timesteps resulting in us recording data at interval $t = 0.01$ time units. We ran these simulations until a time of $t = 1$.

C. Reynolds Number

An important consideration in this study was how the Reynolds number affects simulations and our AI model's ability to reproduce the results of the simulations. The Reynolds number is a dimensionless quantity that expresses the ratio of inertial to viscous forces. The higher the Reynolds number is, the more prevalent the effects of small scale phenomena are to the simulation. This often gives rise to turbulence at high Reynolds numbers. For systems described by MHD equations, there are actually 2 types of Reynolds numbers of interest. They are the kinetic Reynolds number, Re , and the magnetic Reynolds number, Re_m . We define the quantities in our simulation such that these Reynolds numbers are given by

$$Re = 1/\nu, \quad (8)$$

$$Re_m = 1/\eta. \quad (9)$$

The ratio between these two Reynolds numbers is called the magnetic Prandtl number Pr_m defined as

$$Pr_m = \frac{Re_m}{Re} = \frac{\nu}{\eta}. \quad (10)$$

In this study, we sought to characterize how the Reynolds number affects our models and determine if there is a cutoff Reynolds number, after which point, the models' performance degrades considerably. We generally kept $Re = Re_m$ or, equivalently, $Pr_m = 1$ unless otherwise noted and looked at Reynolds number values of 100, 250, 500, 1,000, and 10,000.

One difference between MHD and hydrodynamic simulations is that, compared to the pure hydrodynamic case, much of the magnetic field energy is stored at high wavenumbers which occur at smaller scales. Thus, the models must be able to characterize high frequency features if they are to successfully reproduce the results of the magnetic field evolution.

III. MODELING MHD WITH PINOS

A. PINOs

The goal of a neural operator (NO) is to reproduce the results of an operator given some input fields using neural networks. A common class of operator often studied by NOs are PDEs. To model PDEs, NOs take the coordinates, initial conditions (ICs), boundary conditions (BCs), and coefficient fields as inputs. As outputs, NOs provide the solution of the operator, in this case the PDE, at the desired spacetime coordinates.

There are a variety of different NOs that have been studied in recent works. These include DeepONets, physics informed DeepONets, low-rank neural operators (LNO), graph neural operators (GNO), multipole graph neural operators (MGNO), Fourier neural operators (FNO), factorized Fourier neural operators (fFNO), and PINO [22, 26, 27, 31–36]. In this study we use PINOs.

PINOs are a generic class of NOs that involve using an existing neural operator and employing physics informed methods in the training [26, 27]. Physics informed deep learning methods involves encoding known information about the physical system into the model during training [37–42]. This physics information may include governing PDEs, symmetries, constraint laws, ICs, and BCs. By including such physical knowledge, physics informed methods enable better generalization of the results of deep learning models [42]. In systems where we have a lot of knowledge about the physical system like PDEs, such methods are especially useful as theoretically we could learn from just this physics knowledge. In practice, we add data to help PINOs converge to the correct solution more quickly.

One of the most common ways of encoding this physics into a neural network model is to incorporate physics information into the loss function [37–40]. In other words, violations of these physics laws appear as terms in the loss function that are reduced over time during training. Thus, this technique treats physics laws as soft constraints learned by the neural network as it trains.

For the backbone NO, we selected a variant of fFNO [36] that employed the `TensorLY` [43] package to perform tensor factorization. We call this model a tensor Fourier neural operator (tFNO). The base FNO model [35] applies the fast Fourier transform (FFT) to the data to separate it into its component

frequencies and apply its weights before performing an inverse FFT to convert back to real space. One particular feature of the FNO is its ability to perform zero-shot super-resolution, in which the model predicts on higher resolution data than it was trained on [22, 35]. We hope such properties of the FNO model would allow it to learn the high frequency properties of the MHD equations.

To further augment the model, we utilized factorization with `TensorLY` within the spectral layers of the model, so that it becomes an tFNO. The factorization was found to significantly improve the generalization of the neural network in the initial tests. The decision to use `TensorLY` was inspired by experimental code found in the `GitHub` repository of [26]. We will describe the model architecture in more detail in Section IV B.

B. Applying to MHD Equations

Now let us discuss in more detail how to apply physics informed methods to model the MHD equations with neural operators. There are several aspects to modeling the MHD equations with such methods as denoted by each loss term. These are the data loss \mathcal{L}_{data} , the PDE loss \mathcal{L}_{PDE} , the constraint loss \mathcal{L}_{constr} , the IC loss \mathcal{L}_{IC} , and the BC loss \mathcal{L}_{BC} .

The data loss is modeled by obtaining simulation data and ensuring that the PINO output matches the simulation results. This requires us to produce a large quantity of simulations to provide sufficient training data like those described in Section II B to span the solution space. We will discuss in more detail how we produced a sufficient number of simulations in Section IV A. Then we use the relative mean squared error (MSE) between the simulation and the PINO predictions to define the value of the data loss \mathcal{L}_{data} .

The PDE loss describes the violations of the time evolution PDEs of the PINO outputs. Specifically, we encode these time evolution PDEs as part of the loss function. This requires us to represent the spatial and temporal derivatives of the output fields. Although some NOs are able to employ the automatic differentiation of the deep learning framework to calculate such derivatives [32], this method is too memory intensive for the tFNO architecture. Instead, we employ Fourier differentiation to represent the spacial derivatives, which computes highly accurate derivative values while conveniently assuming periodic BC that exists in our problem. For time derivatives, we use second order finite differencing. We note that such a time differencing technique cannot be used during the original simulation as this requires knowledge of future times to compute the time derivative of the current time.

Specifically, the PDEs we modeled with this technique were Equation 1 for velocity evolution and Equation 5 for magnetic potential evolution. In this case, the model has a total of 3 output fields in 2D, the velocity in the x direction u , the velocity in the y direction v , and the magnetic potential A . We also tested replacing the magnetic vector potential evolution with the magnetic field evolution of Equation 2, which results in 4 output fields in 2D. The fields in this case are the velocity in the x direction u , the velocity in the y direction v , the magnetic field in the x direction B_x , and the magnetic field

in the y direction B_y . We note that in testing, the former representation of the MHD equations produced better results. The PDE loss \mathcal{L}_{PDE} is then defined as the MSE loss between zero and the PDE, after putting all the terms on the same side of the equation.

Due to the complexity of both representations of the MHD equations, we tested the PDE loss on the data produced by the simulations. We found that the loss was small, albeit nonzero. This nonzero PDE loss was expected since the numerical methods for computing the derivatives during the simulation differs from those of computing the derivatives of the PDE during the loss function. Some particular notable differences are having fewer time steps in the output data than was used during the simulation, using different time derivative methods (e.g., RK4 during simulation vs second order finite differencing during the loss computation), and lacking dealiasing in the spatial derivatives in the PDE loss function.

The constraint loss illustrates the deviations of the elliptic constraint equations of the MHD equations. Specifically, these refer to the velocity divergence free condition of Equation 3 and the magnetic divergence free condition of Equation 4. We implemented these constraints similarly to the time evolution equations in the PDE loss, but without any time derivative terms. The constraint loss \mathcal{L}_{constr} is then the MSE between each of the constraint equations and zero. We note that we are representing the magnetic fields by the magnetic potential, the magnetic field divergence free condition is satisfied up to the numerical precision of the curl operator regardless of the prediction of the neural network. However, we still include the term for completeness and this condition is not guaranteed to be nonzero if we are trying to compute the magnetic fields directly.

The IC loss tells the model to associate the input field with the output at $t = 0$. Although this function can often be achieved with the data loss alone, the IC loss emphasizes the importance of predicting the correct IC and enables training in the absence of data. Both the significance of the IC and the ability to train without data stem from the PDE loss term. Theoretically, one can train by correctly predicting the IC, the BCs, and evolving the PDE correctly forward in time, although in practice, data helps the model converge more quickly. However, an incorrect IC results in the PDE evolving the wrong data forward in time. Thus, we add in the IC as its own term to encourage the model to first compute the IC correctly before learning the time evolution later in training. We calculate the IC loss \mathcal{L}_{IC} by taking the input fields and computing the relative MSE between said input fields and the outputs fields at $t = 0$.

Finally, the BC loss \mathcal{L}_{BC} describes the violations of the boundary terms. In our case, the tFNO model architecture ensures that we have the desired periodic BC. Therefore, we do not use such a term in our model. However, we mention this term for generality because not all BCs and the periodicity of the tFNO architecture can be removed by zero padding the inputs along the desired non-periodic axis.

In physics informed deep learning methods, one must be careful when combining fields of different magnitudes to ensure they all have an equal contribution to the loss. Therefore,

our model has the ability to normalize the input fields and denormalize the output fields by multiplying by predetermined constants. Moreover, we assign a weight to each term when combining loss terms for different fields and equation. We add additional weights when combining different losses. Thus, our loss \mathcal{L} is given as

$$\mathcal{L} = w_{\text{data}}\mathcal{L}_{\text{data}} + w_{\text{PDE}}\mathcal{L}_{\text{PDE}} + w_{\text{constr}}\mathcal{L}_{\text{constr}} + w_{\text{IC}}\mathcal{L}_{\text{IC}}, \quad (11)$$

where w_{data} is the data weight, w_{PDE} is the PDE weight, w_{constr} is the constraint weight, and w_{IC} is the IC weight.

IV. METHODS

A. Data Generation

To generate the training data, we first needed to produce initial data before running it in the simulations described in Section II B. These initial data fields are produced using Gaussian random field (GRF) method similar to [27], in which the kernel was transformed into Fourier space to obey our desired periodic BCs. Specifically, we used the radial basis function kernel (RBF) to produce smooth initial fields. This kernel k_l is defined as

$$k_l(x_1, x_2) = \exp\left(-\frac{\|x_1 - x_2\|^2}{2l^2}\right), \quad (12)$$

where l is the length scale of typical spatial deviations in the data. We used $l = 0.1$ for all fields in this work unless otherwise stated. We also needed to ensure that the velocity and magnetic fields are both divergence free. Therefore, we produced 2 initial data fields, the vorticity potential, ψ , and the magnetic potential A . We defined ψ such that

$$\mathbf{v} = \nabla \times \psi, \quad (13)$$

which guarantees the velocity fields are divergence free initially. The magnetic potential A is defined in Equation (6) in a similar manner to prevent the presence of divergences in the initial magnetic fields.

We multiplied the resulting initial data fields by a constant to ensure that the resulting fields have appropriate magnitude and are numerically stable. For example, we need to prevent Courant-Friedrichs-Lewy (CFL) condition violations, which can occur if the velocities are too high for a given resolution and timestep choice [44]. Numerical instabilities can also occur if the initial magnetic potential values are too high and may cause the simulation to fail. We chose these constants to be $c_\psi = 0.1$ for the vorticity potential ψ and $c_A = 0.005$ for the magnetic potential A .

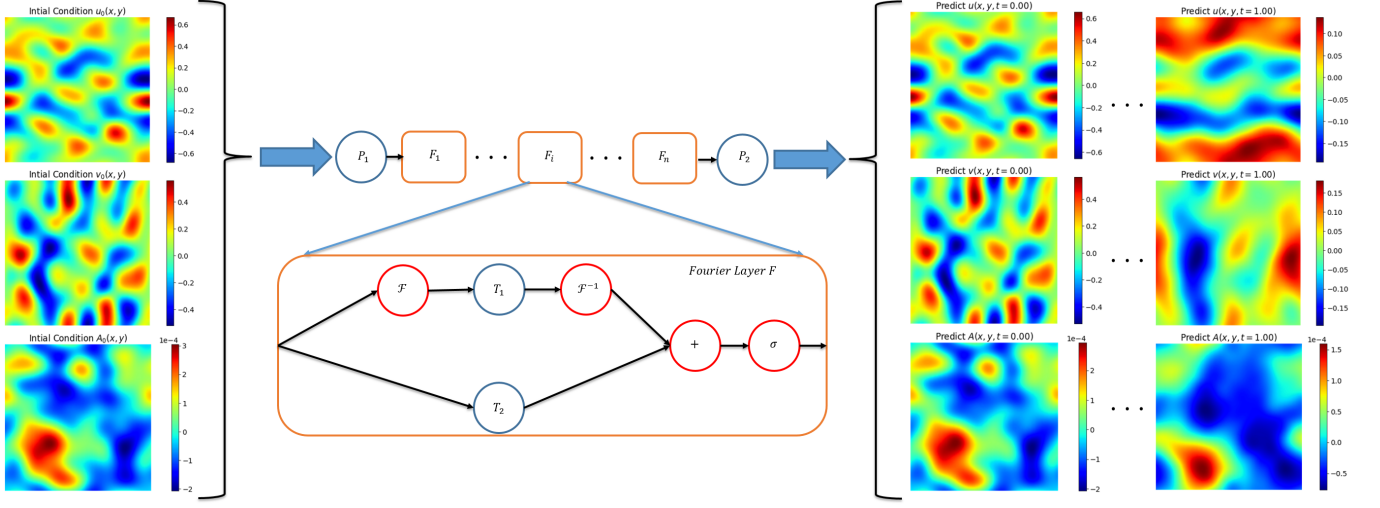


Figure 1 : Architecture: Schematic representation of the architecture of our PINO models, which use the `TensorLY` [43] package to perform tensor factorization, thereby using tensor Fourier neural operators (tFNO) as the backbone of our AI models. On the far left, we display sample input fields that are fed into our PINO, which are composed of the u , v , and A initial conditions (ICs). To the right of the input fields, we illustrate how the data is transformed as it goes through the model. First, this input data is lifted into a higher dimension representation by the neural network, P_1 . Then, the data enters a series of Fourier layers labeled $\{F_1, \dots, F_i, \dots, F_n\}$. The inset zooms into one of these Fourier layers. In the inset, labelled as "*Fourier Layer F*", we apply a series of operations that consist of non-local integral operators and nonlinear activation functions. Specifically, T_1 represents a linear transform that employs CP decomposed tensors as weights, T_2 represents a local linear transform, and σ represents a nonlinear activation function. \mathcal{F} and \mathcal{F}^{-1} stand for Fourier transform and inverse Fourier transform, respectively. Eventually, the neural network P_2 projects back into position space, producing the output shown on the right panels, which describe the time evolution of the system. These outputs are presented on the right of the image for the output fields u , v , and A at times that range from $t = 0$ to $t = 1$.

B. Model Architecture

A schematic of the tFNO models utilized in this study is presented in Figure 1. The size and dimensions of the model can be described by 3 hyperparameters—the width, the number of Fourier modes, and the number of layers. We used 4 layers for all models in this work. The width and number of Fourier modes were the same across all layers of the model in this work and were both set to 8 unless stated otherwise. Although we suspect that we could get better results by increasing these hyperparameters, especially the number of Fourier modes which may have helped the models reproduce small scale features in the flow, doing so proved too memory intensive for our GPUs.

We factorized the weight tensors within the spectral layers with `TensorLY` to improve generalizability. Specifically, we used a canonical polyadic tensor decomposition [45] with a rank of 0.5 to perform this factorization. Prior to producing the outputs, the models employ a fully connected layer of width 128.

In addition, the model normalizes its data internally by dividing by a constant input normalization factor to ensure that magnitude varying inputs are treated the same way. In particular, the magnitude of the magnetic potential A was considerably less than that of the velocity fields u and v . Similarly, we multiplied the output by a constant output normalization factor to alleviate the tFNO model from having to produce results with significantly different magnitudes. For this work, we used the same value for the input and output normalization fields of 1 for the velocity fields and 0.00025 for the magnetic potential

A . Finally, we selected the Gaussian error linear unit (GELU) for the nonlinearity of these models [46].

C. Training

We trained these models using the `PyTorch` deep learning framework [47]. We used an AdamW optimizer [48] with a weight decay value of 0.1. This optimizer used $\beta_1 = 0.9$, $\beta_2 = 0.999$, and an initial learning rate of 0.001.

We employed a multistep scheduler to reduce the learning rate over time to better fine tune the PINO. This scheduler had a gamma value of 0.5, though the milestones varied between runs. It was common to begin training for 150 epochs to verify that PINO was working as expected. For these shorter runs, a common set of scheduler milestones was [25, 50, 75, 100, 125, 150]. We would then load a checkpoint of these shorter runs and re-train the model for 1000 epochs. A sample set of scheduler milestones that was used for the longer 1000 epoch training sessions was [10, 25, 100, 250, 500, 750, 1000]. We logged specific hyperparameters used in training each PINO using `WandB` [49] for reproducibility.

To accelerate the training, we would employ transfer learning across different Reynolds number Re . Specifically, we trained the $Re = 250$ model from scratch, then would use it or other models that have finished training to initialize the weights of new PINOs that seek to model different Re . In turn, this transfer learning saved considerable time when training new models. Some models that trained on a significant num-

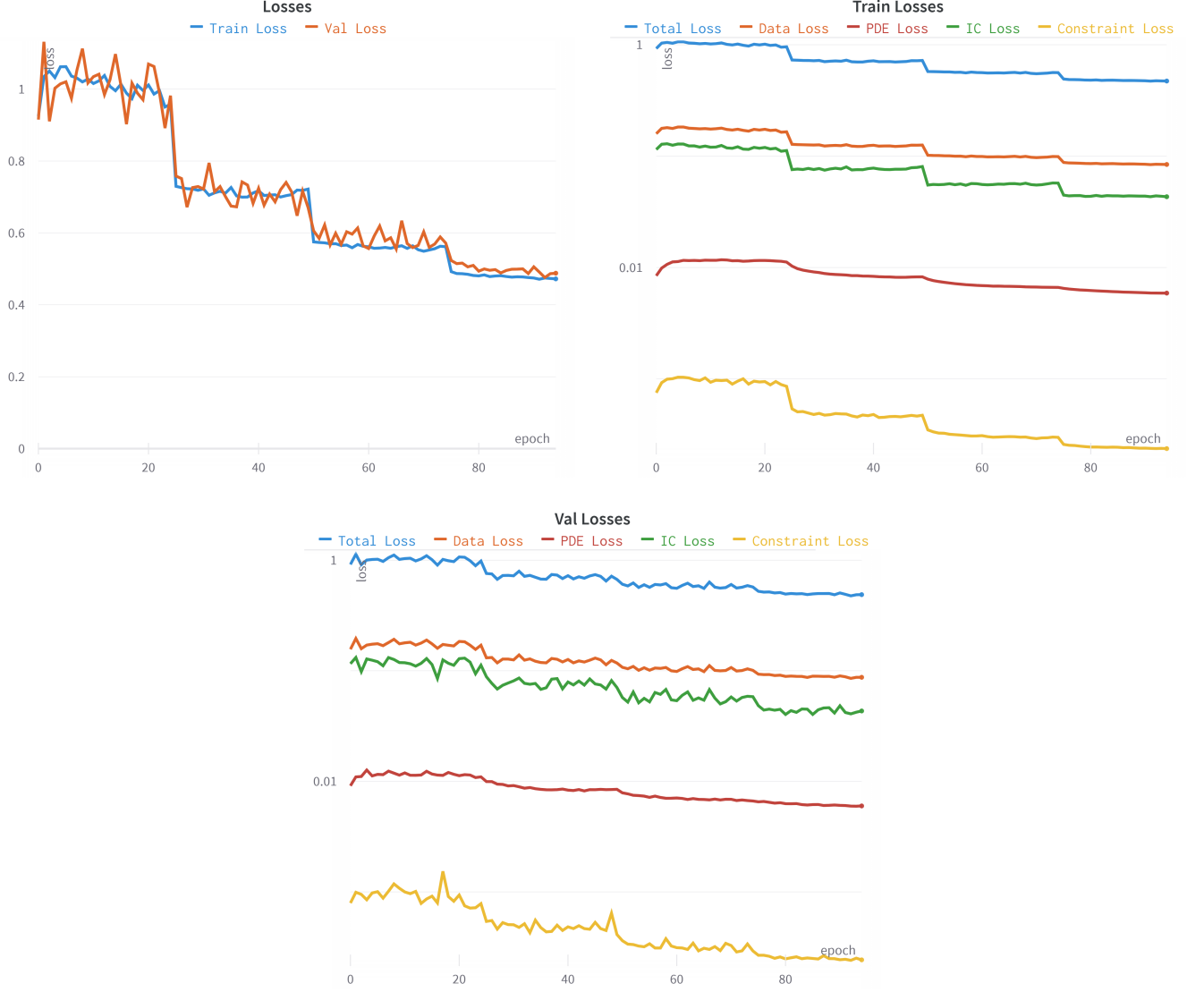


Figure 2 : Loss curves for $Re = 100$ simulation: Top-left panel: total loss for the training and validation data on a linear scale. Top-right panel: training losses for each of the different types of losses we track—total loss, data loss, PDE loss, IC loss, and constraint loss. Bottom panel: same losses as in the top panels, but for the validation data. To illustrate the different scales of these losses, the bottom panel use a log scale for the y-axis. The decrease in loss every 25 epochs occurs due to the scheduler changing the training rate at those epochs. Also, this case did not train from scratch, but rather started from a previous checkpoint of training on this dataset, resulting in a low initial loss value.

ber of simulations such as the $Re = 100$, $Re = 1,000$, and $Re = 10,000$ models, did not complete the full number of epochs they set out to train. Such models would normally train for around 100 epochs, though some trained for fewer. For these models, we would use the most recent checkpoint for reporting results.

We set most of the weight hyperparameters of the various loss terms to 1 with a few notable exceptions. We set the weight of the magnetic potential evolution equation loss w_{DA} to 10^6 as the magnitude of the term was small compared to that of the other evolution equations. In addition, we used a value of the constraint loss weight w_{constr} of 10. For most of the models, we selected $w_{data} = 5$ as our data loss weight.

However, we used $w_{data} = 1$ for the $Re = 500$ case to prevent overfitting.

In Figure 2, we display some characteristic loss curves for the training for the models $Re = 100$ PINO models.

D. Computational Resources

For the training and testing of the models in this study, we used the V100 GPUs on PSC’s Bridges-2 cluster. We primarily used the 16 GB variant of these GPUs, though some cases utilized the 32 GB variation. To generate the training data, we utilized the CPUs on the Bridges-2 cluster’s GPU nodes. We

used a single GPU node for this process, which has two Intel Xeon Gold 6248 "Cascade Lake" CPUs, which have 20 cores, 2.50-3.90GHz, 27.5 MB LLC, 6 memory channels each.

E. Evaluation Criteria

To evaluate the performance of our PINO models, we look at the relative MSE. This allows us to compare errors of the various fields despite them differing in magnitude. We report the relative MSE for the predictions the PINOs on the test dataset for each field of interest. In addition, we compute the total relative MSE, MSE_{tot} , for our PINOs on this data which we defined as

$$MSE_{tot} = MSE_u + MSE_v + MSE_A, \quad (14)$$

where MSE_u , MSE_v , and MSE_A are the MSE values of the u , v , and A fields respectively. In addition, we computed the kinetic energy spectra $E_{kin}(k)$ and magnetic energy spectra, $E_{mag}(k)$, of the PINO predictions and the ground truth simulations. This allowed us to compare how the models perform at various scales as specified by the wavenumber k .

V. RESULTS

Here we present results for the accuracy with which our PINO models solve the MHD equations, and then compare these AI predictions with high performance computing MHD simulations. These simulations are evolved in the time domain $t \in [0, 1]$. We present results for a broad range of Reynolds number Re , summarized in Table I. Our PINO simulations and traditional MHD simulations are compared throughout their entire evolution, and then we take a snapshot of their evolution at $t = 1$. We do this to capture the largest discrepancy between AI-driven simulations and traditional PDE solvers at a time where numerical errors and other discrepancies between these methodologies are maximized.

The first set of results for MHD simulations with Reynolds number $Re = 100$ are presented in Figure 3 at time $t = 1$. These results show that our PINO models can accurately reproduce the dynamical evolution of the MHD equations under these conditions, reporting a relative total MSE for the validation dataset of 0.0931. Moreover, every field of interest was predicted quite accurately with relative MSE values of 0.0242, 0.0263, and 0.0426 for the u , v , and A fields, respectively.

Let us now examine the $Re = 250$ results presented in Figure 4. Therein we observe that the overall agreement between the PINO predictions and the simulations is quite good at time $t = 1$. Quantitatively, we find a total relative MSE of 0.4279 distributed as 0.1081 for u , 0.1174 for v , and 0.2025 for A . We notice that PINOs have the most difficulty reproducing the results of magnetic potential A . However, we should keep in mind that the $Re = 250$ used significantly less training data than the $Re = 100$ case. A fairer comparison would be the $Re = 500$ results which were generated after training our

PINO model with the same amount of data as the $Re = 250$ case. But before doing so, let us look at the higher resolution $Re = 250$ case with $N = 256^2$ grid points.

In Figure 5, we present the results of the $Re = 250$ models with a resolution of $N = 256^2$ grid points. These results appear to indicate very good agreement between PINO predictions and the simulation for this higher resolution version of the $Re = 250$ PINO model. Like the lower resolution version of the $Re = 250$ model, we observe some deviations from the simulations under closer inspection, but they are harder to spot in the higher resolution case. Calculating the MSE, we found that the relative total MSE of 0.3304, with the MSE distribution being similar to the previous cases. This MSE value is somewhat less than that of the low resolution $Re = 250$ case, though the difference is not significant. It is unclear if we should attribute this improvement to the increased inherent additional data that comes with higher resolution, or whether there exists some issue with the $N = 128^2$ grid points simulation preventing it from fully resolving the MHD at $Re = 250$.

Figure 6 presents results for the $Re = 500$ PINO models. We notice that while PINOs capture large scale features well, they do not accurately describe smaller scale features. The magnetic potential A is the quantity that has the most noticeable discrepancy between PINO predictions and ground truth simulations. The total MSE of 0.7972 also indicates a significantly poor performance compared to lower Reynolds number cases. The magnetic potential A performed worse than the velocity fields in this case as well.

The $Re = 1,000$ results presented in Figure 7 indicate similar effects to the $Re = 500$ case. Mainly, the PINO models are able to reproduce large scale features at high Reynolds numbers, but struggle with the finer features, especially for the magnetic field. The MSE for the $Re = 1,000$ case was found to be 0.7361 with the poorest performance coming from the magnetic potential A . This MSE is actually less than that of the $Re = 500$ models, which may be due to having more training data for the $Re = 1,000$. With that said, the flow properties of the $Re = 1,000$ are likely similar to that of the $Re = 500$ flow as the performance of the PINO models was comparable across these Reynolds numbers.

Finally, we present the results of the $Re = 10,000$ case in Figure 8. We observe that the ground truth simulation data appears turbulent especially in the magnetic field. It may have been turbulent to such an extent that we suspect this simulation was not fully resolved for the 128^2 grid points used in the simulations. We observe that for the velocity fields, the PINO model was able to resolve some of the large scale features of the flow, but struggled to reproduce many of the detailed features. One particular feature that the PINO misses is the small scale fluctuations in the velocity field that likely result from strong magnetic fields in those areas. In other words, the PINO fails to model the effect of the magnetic field on the fluid motion. For the magnetic potential, the PINO model appears to miss most of the important features at first glance. If we look more closely, we observe that the PINO appears, to some extent, to reproduce the mean field value over some very large regions. However, this comes at the cost of missing any sort of interesting details in the magnetic field. Accordingly, the MSE

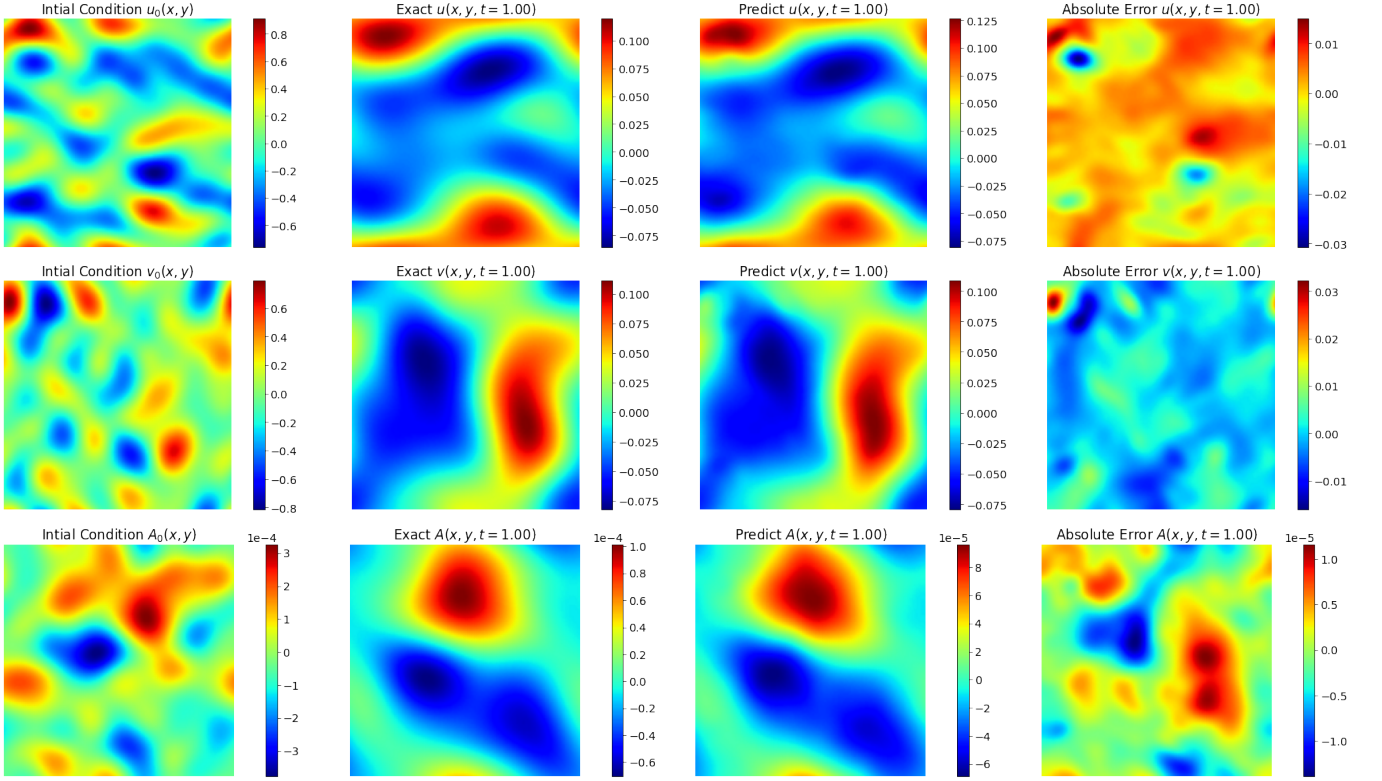


Figure 3 : $Re = 100$ MHD Simulations Results of the PINO model on sample test data from the $Re = 100$ simulations. The rows correspond to the fields of interest with the velocity in the x direction u , the velocity in the y direction v , and the magnetic potential A being the quantities featured in the top, middle, bottom rows, respectively. The far left column depicts the initial condition given to the PINO model. The center left column shows the ground truth at time $t = 1$. In the center right column, we present the PINO predictions at time $t = 1$. The far right column error between the ground truth and the PINO predictions at $t = 1$.

Table I : Summary of Results: Presents the results of our PINO models. The Re column displays the Reynolds number of the model. The Resolution column provides the resolution of the model. The N_{train} and N_{test} columns tell us how many simulations were used in training and testing respectively for each PINO. The MSE u , MSE v , and MSE A give us the relative MSE values of the u , v , and A fields respectively. The far right column, MSE Total, lists the sum of the MSE values of the u , v , and A fields.

Re	Resolution	N_{train}	N_{test}	MSE u	MSE v	MSE A	MSE Total
100	128^2	700	55	0.0242	0.0263	0.0426	0.0931
250	128^2	90	10	0.1081	0.1174	0.2025	0.4279
250	256^2	90	10	0.0809	0.0966	0.1528	0.3304
500	128^2	90	10	0.2091	0.2213	0.3668	0.7972
1,000	128^2	700	55	0.1877	0.1914	0.3569	0.7361
10,000	128^2	440	25	0.2993	0.3048	0.5738	1.1779

was highest for this case with a value of 1.1779. As with the other cases, the vector potential had the highest MSE value.

In summary, Figures 3 to 8 show that our PINO models can successfully reproduce large scale features of MHD simulations, but had difficulty resolving detailed features for large Reynolds numbers, especially for the magnetic potential, which is known to store its energy at higher wavenumbers. Therefore, we analyzed the magnetic and kinetic energy spectra of the simulations in Figure 9. Therein we observe that for both the kinetic and magnetic energy spectra, the PINO models performed well at low wavenumbers k . However, the PINOs were not able to accurately reproduce the energy spectra at high wavenum-

bers. Interestingly, at low Re , the PINOs tended to overshoot the ground truth energies at high wavenumbers. While at high Re , the PINOs tended to undershoot the ground truth energies at high wavenumbers. Moreover, large Reynolds number simulations usually store more energy at higher wavenumbers. This is especially true for the magnetic energy, which tends to peak at later wavenumbers in higher Re simulations. Therefore, the spectra plots in Figure 9 indicate that the difficulties the PINOs had in reproducing the simulations at high Re and the magnetic potential field A may stem from their relatively poor performance at high wavenumbers. Therefore, future work should focus on developing methods that enable PINOs to capture

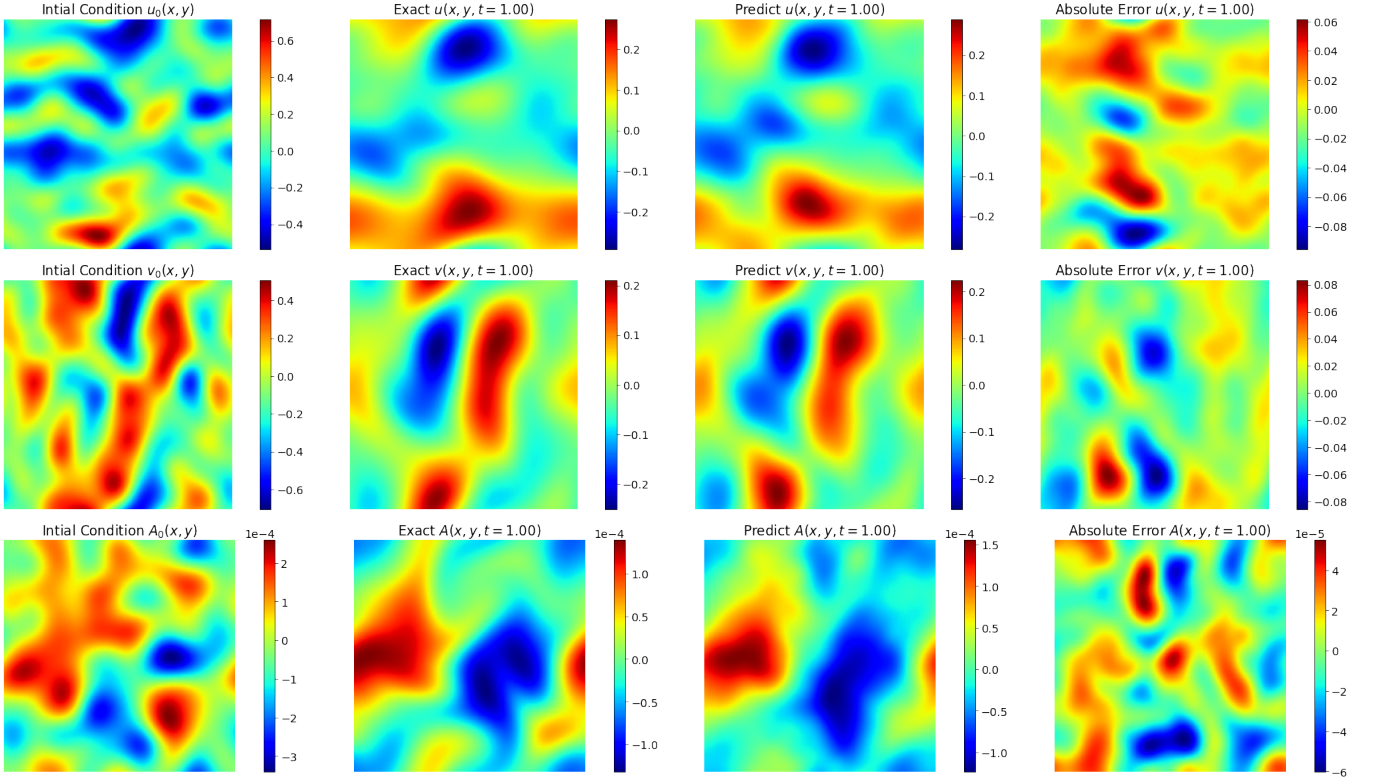


Figure 4 : $Re = 250$ MHD Simulations As Figure 3 but now for a test set from the $Re = 250$ simulations.

data features contained at high wavenumbers.

VI. CONCLUSIONS

In this work we presented the first application of PINOs to model MHD simulations for a variety of initial conditions and Reynolds numbers. Our PINO models were able to accurately describe MHD simulations at Reynolds numbers $Re \leq 250$. We also showed that detailed structure in MHD simulations with $Re > 500$ —in particular the magnetic potential, A , which we used to evolve the magnetic fields—is not fully resolved by our PINO models. We explored this issue by analyzing the energy spectra of the MHD simulations and PINOs, and found that this issue may likely stem from the PINOs’ difficulty in learning physics contained at high wavenumbers.

We suggest that future work should focus on optimizing neural operators at these high wavenumbers. One suggestion would be to increase the number of Fourier modes used by our tFNO backend. While in this study we have considered 8 Fourier modes, recent work involving FNOs for hydrodynamic turbulence modeling have had success with using 20 Fourier modes [25]. One should be cautious, however, since using too many Fourier modes may also introduce numerical noise and complicate the resolution of small scale features in the simulation data.

Another suggestion is to develop methods that enable PINOs to learn the turbulence statistics of the MHD simulation in

addition to the flow. For example, one could incorporate the kinetic and magnetic energy spectra into the loss function and weigh in the contribution of the high wavenumber portions of the spectrum appropriately. Through this approach, PINOs may predict the flow with the correct turbulent characteristics even if they are unable to accurately model the details of the flow. We expect that this work may provide a stepping stone to other AI practitioners who are developing novel methods to model turbulent MHD simulations.

ACKNOWLEDGMENTS

This material is based upon work supported by Laboratory Directed Research and Development (LDRD) funding from Argonne National Laboratory, provided by the Director, Office of Science, of the U.S. Department of Energy under Contract No. DE-AC02-06CH11357. This research used resources of the Argonne Leadership Computing Facility, which is a DOE Office of Science User Facility supported under Contract DE-AC02-06CH11357. S.R. and E.A.H. gratefully acknowledge National Science Foundation award OAC-1931561. This work used the Extreme Science and Engineering Discovery Environment (XSEDE), which is supported by National Science Foundation grant number ACI-1548562. This work used the Extreme Science and Engineering Discovery Environment (XSEDE) Bridges-2 at the Pittsburgh Supercomputing Center through allocation TG-PHY160053. This research used

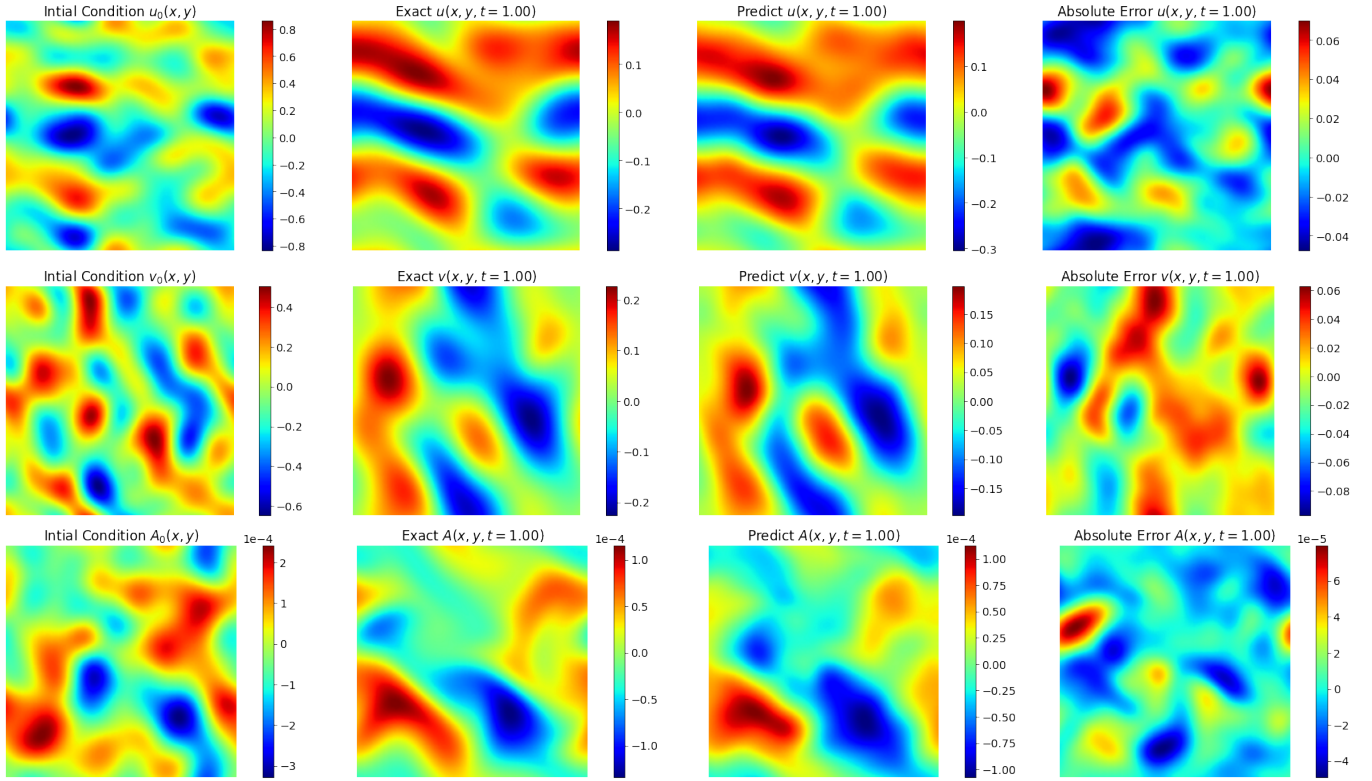


Figure 5 : $Re = 250$ $N = 256^2$ MHD Simulations As Figure 3 but now for a test set from the the $Re = 250$ simulations with resolution of $N = 256^2$ grid points.

the Delta advanced computing and data resource which is supported by the National Science Foundation (award OAC-

2005572) and the State of Illinois. Delta is a joint effort of the University of Illinois Urbana-Champaign and its National Center for Supercomputing Applications.

-
- [1] A. Beresnyak, *Living Reviews in Computational Astrophysics* **5**, 2 (2019)
 - [2] A. A. Schekochihin, *Journal of Plasma Physics* **88**, 155880501 (2022)
 - [3] A. Pouquet, D. Rosenberg, J. Stawarz, and R. Marino, *Earth and Space Science* **6**, 351 (2019), <https://agupubs.onlinelibrary.wiley.com/doi/pdf/10.1029/2018EA000432>
 - [4] K. Kiuchi, P. Cerdá-Durán, K. Kyutoku, Y. Sekiguchi, and M. Shibata, *Phys. Rev. D* **92**, 124034 (2015)
 - [5] A. Beresnyak, *Phys. Rev. Lett.* **108**, 035002 (2012)
 - [6] A. Beresnyak and A. Lazarian, Mhd turbulence, turbulent dynamo and applications, in *Magnetic Fields in Diffuse Media*, edited by A. Lazarian, E. M. de Gouveia Dal Pino, and C. Melioli (Springer Berlin Heidelberg, Berlin, Heidelberg, 2015) pp. 163–226
 - [7] P. Grete, *Large eddy simulations of compressible magnetohydrodynamic turbulence*, Ph.D. thesis, Max-Planck-Institut für Sonnensystemforschung (2017)
 - [8] P. Grete, D. G. Vlaykov, W. Schmidt, D. R. G. Schleicher, and C. Federrath, *New Journal of Physics* **17**, 023070 (2015)
 - [9] P. Grete, D. G. Vlaykov, W. Schmidt, and D. R. G. Schleicher, *Physics of Plasmas* **23**, 062317 (2016), <https://doi.org/10.1063/1.4954304>
 - [10] D. G. Vlaykov, P. Grete, W. Schmidt, and D. R. G. Schleicher, *Physics of Plasmas* **23**, 062316 (2016), <https://doi.org/10.1063/1.4954303>
 - [11] P. Grete, D. G. Vlaykov, W. Schmidt, and D. R. G. Schleicher, *Phys. Rev. E* **95**, 033206 (2017)
 - [12] P. Grete, B. W. O’Shea, K. Beckwith, W. Schmidt, and A. Christlieb, *Physics of Plasmas* **24**, 092311 (2017), <https://doi.org/10.1063/1.4990613>
 - [13] M. Kessar, G. Balarac, and F. Plunian, *Physics of Plasmas* **23**, 102305 (2016), <https://doi.org/10.1063/1.4964782>
 - [14] R. Aguilera-Miret, D. Viganò, and C. Palenzuela, *The Astrophysical Journal Letters* **926**, L31 (2022)
 - [15] C. Palenzuela, R. Aguilera-Miret, F. Carrasco, R. Ciolfi, J. V. Kalinani, W. Kastaun, B. Miñano, and D. Viganò, *Phys. Rev. D* **106**, 023013 (2022)
 - [16] D. Viganò, R. Aguilera-Miret, and C. Palenzuela, *Physics of Fluids* **31**, 105102 (2019)
 - [17] F. Carrasco, D. Viganò, and C. Palenzuela, *Phys. Rev. D* **101**, 063003 (2020)
 - [18] D. Viganò, R. Aguilera-Miret, F. Carrasco, B. Miñano, and C. Palenzuela, *Phys. Rev. D* **101**, 123019 (2020)
 - [19] D. Radice, *Symmetry* **12**, 10.3390/sym12081249 (2020)

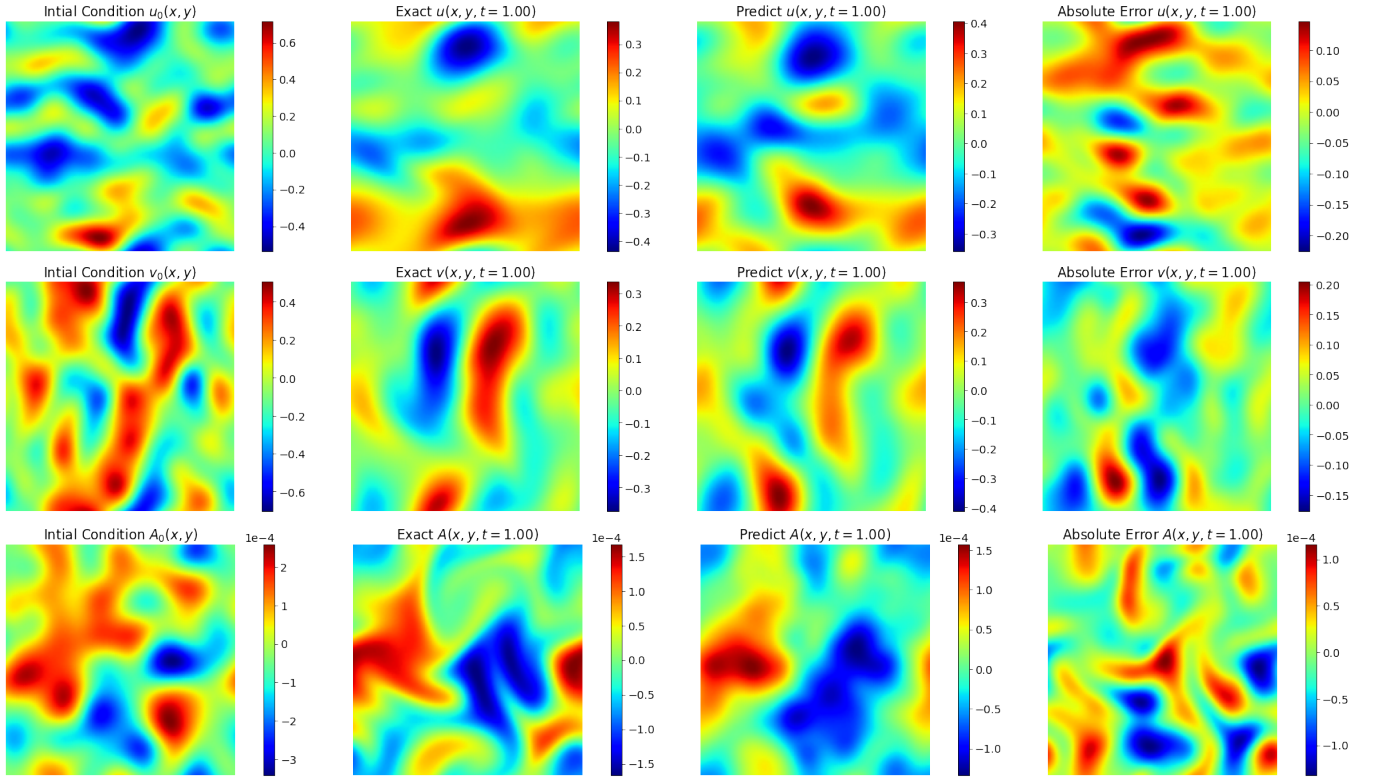


Figure 6 : $Re = 500$ MHD Simulations As Figure 3 but now for a test set from the $Re = 500$ simulations.

- [20] S. G. Rosofsky and E. A. Huerta, *Phys. Rev. D* **101**, 084024 (2020)
- [21] P. I. Karpov, C. Huang, I. Sitdikov, C. L. Fryer, S. Woosley, and G. Pilania, *The Astrophysical Journal* **940**, 26 (2022)
- [22] N. Kovachki, Z. Li, B. Liu, K. Azizzadenesheli, K. Bhattacharya, A. Stuart, and A. Anandkumar, arXiv e-prints, arXiv:2108.08481 (2021), arXiv:2108.08481 [cs.LG]
- [23] W. Peng, Z. Yuan, Z. Li, and J. Wang, *Linear attention coupled fourier neural operator for simulation of three-dimensional turbulence* (2022)
- [24] W. Peng, Z. Yuan, and J. Wang, *Physics of Fluids* **34**, 025111 (2022), <https://doi.org/10.1063/5.0079302>
- [25] Z. Li, W. Peng, Z. Yuan, and J. Wang, *Theoretical and Applied Mechanics Letters*, 100389 (2022)
- [26] Z. Li, H. Zheng, N. Kovachki, D. Jin, H. Chen, B. Liu, K. Azizzadenesheli, and A. Anandkumar, arXiv e-prints, arXiv:2111.03794 (2021), arXiv:2111.03794 [cs.LG]
- [27] S. G. Rosofsky, H. Al Majed, and E. A. Huerta, arXiv e-prints, arXiv:2203.12634 (2022), arXiv:2203.12634 [physics.comp-ph]
- [28] A. Dedner, F. Kemm, D. Kröner, C.-D. Munz, T. Schnitzer, and M. Wessenberg, *Journal of Computational Physics* **175**, 645 (2002)
- [29] P. Mocz, M. Vogelsberger, and L. Hernquist, *Monthly Notices of the Royal Astronomical Society* **442**, 43 (2014), <https://academic.oup.com/mnras/article-pdf/442/1/43/4072384/stu865.pdf>
- [30] K. J. Burns, G. M. Vasil, J. S. Oishi, D. Lecoanet, and B. P. Brown, *Physical Review Research* **2**, 023068 (2020), arXiv:1905.10388 [astro-ph.IM]
- [31] L. Lu, P. Jin, G. Pang, Z. Zhang, and G. E. Karniadakis, *Nature Machine Intelligence* **3**, 218–229 (2021)
- [32] S. Wang, H. Wang, and P. Perdikaris, *Science Advances* **7**, eabi8605 (2021)
- [33] Z. Li, N. Kovachki, K. Azizzadenesheli, B. Liu, K. Bhattacharya, A. Stuart, and A. Anandkumar, Neural operator: Graph kernel network for partial differential equations (2020), arXiv:2003.03485 [cs.LG]
- [34] Z. Li, N. B. Kovachki, K. Azizzadenesheli, B. Liu, K. Bhattacharya, A. M. Stuart, and A. Anandkumar, *CoRR abs/2006.09535* (2020), 2006.09535
- [35] Z. Li, N. Kovachki, K. Azizzadenesheli, B. Liu, K. Bhattacharya, A. Stuart, and A. Anandkumar, Fourier neural operator for parametric partial differential equations (2020), arXiv:2010.08895 [cs.LG]
- [36] A. Tran, A. Mathews, L. Xie, and C. S. Ong, arXiv e-prints, arXiv:2111.13802 (2021), arXiv:2111.13802 [cs.LG]
- [37] M. Raissi, P. Perdikaris, and G. E. Karniadakis, Physics informed deep learning (part i): Data-driven solutions of nonlinear partial differential equations (2017), arXiv:1711.10561 [cs.AI]
- [38] M. Raissi, P. Perdikaris, and G. E. Karniadakis, Physics informed deep learning (part ii): Data-driven discovery of nonlinear partial differential equations (2017), arXiv:1711.10566 [cs.AI]
- [39] M. Raissi, P. Perdikaris, and G. Karniadakis, *Journal of Computational Physics* **378**, 686 (2019)
- [40] G. Pang, L. Lu, and G. E. Karniadakis, *SIAM Journal on Scientific Computing* **41**, A2603 (2019), <https://doi.org/10.1137/18M1229845>
- [41] L. Lu, X. Meng, Z. Mao, and G. E. Karniadakis, *SIAM Review* **63**, 208 (2021)
- [42] G. E. Karniadakis, I. G. Kevrekidis, L. Lu, P. Perdikaris, S. Wang, and L. Yang, *Nature Reviews Physics* **3**, 422 (2021)

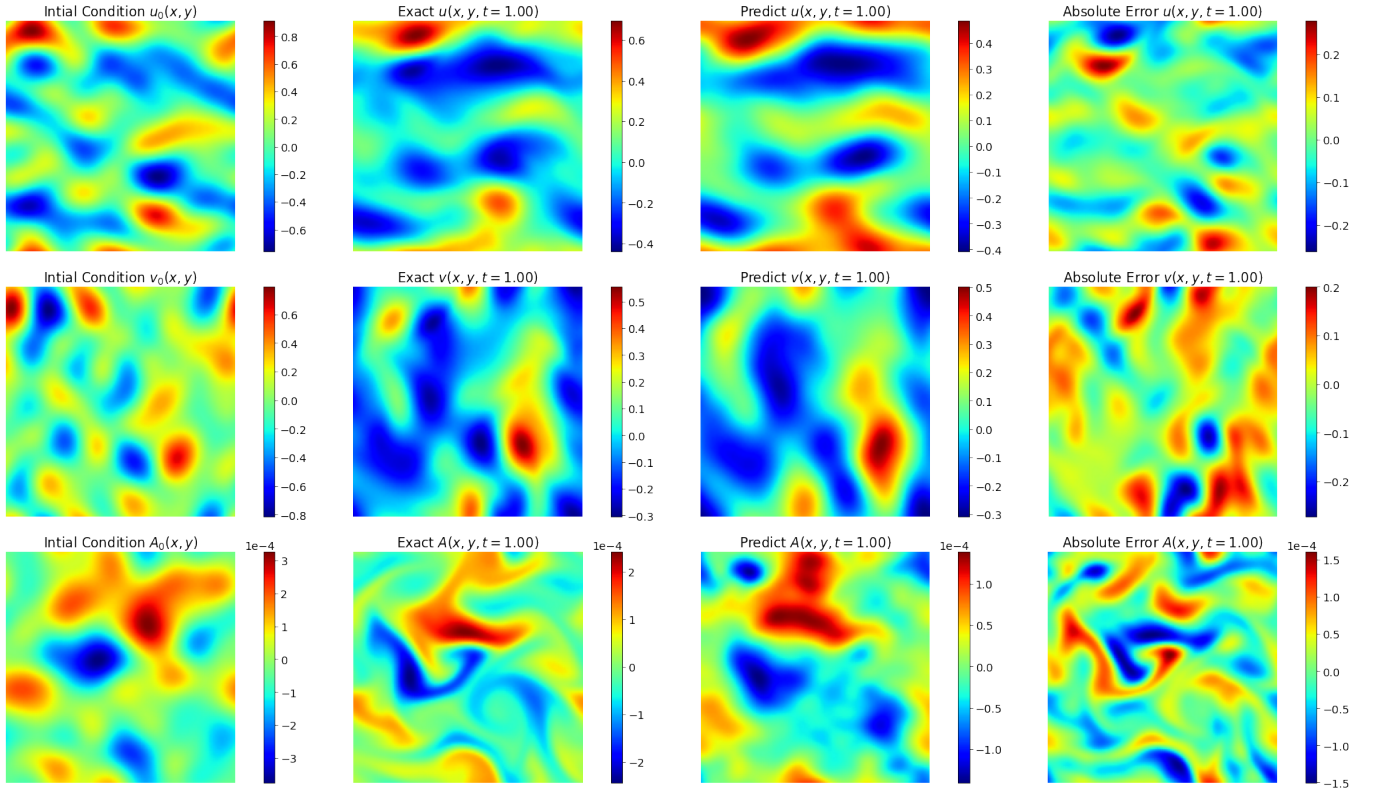


Figure 7 : $Re = 1,000$ MHD Simulations As Figure 3 but now for a test set from the $Re = 1,000$ simulations.

- [43] J. Kossaifi, Y. Panagakis, A. Anandkumar, and M. Pantic, [Journal of Machine Learning Research](#) **20**, 1 (2019)
- [44] R. Courant, K. Friedrichs, and H. Lewy, [Mathematische Annalen](#) **100**, 32 (1928)
- [45] N. B. Erichson, K. Manohar, S. L. Brunton, and J. N. Kutz, [Machine Learning: Science and Technology](#) **1**, 025012 (2020)
- [46] D. Hendrycks and K. Gimpel, Gaussian error linear units (gelus) (2016), [arXiv:1606.08415 \[cs.LG\]](#)
- [47] A. Paszke, S. Gross, S. Chintala, G. Chanan, E. Yang, Z. DeVito, Z. Lin, A. Desmaison, L. Antiga, and A. Lerer, in [NIPS 2017 Workshop on Autodiff](#) (2017)
- [48] I. Loshchilov and F. Hutter, Decoupled weight decay regularization (2017), [arXiv:1711.05101 \[cs.LG\]](#)
- [49] L. Biewald, [Experiment tracking with weights and biases](#) (2020), software available from wandb.com

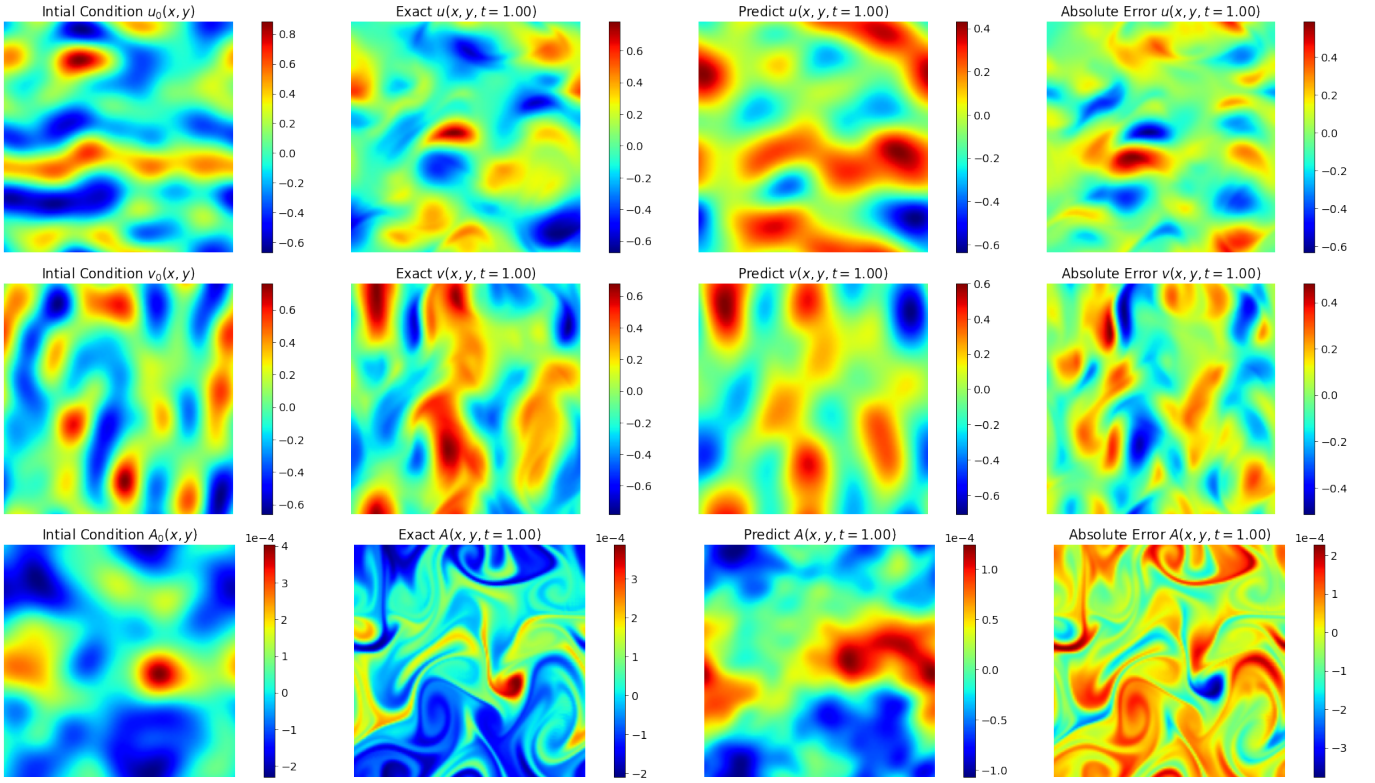


Figure 8 : $Re = 10,000$ MHD Simulations As Figure 3 but now for a test set from the $Re = 10,000$ simulations.

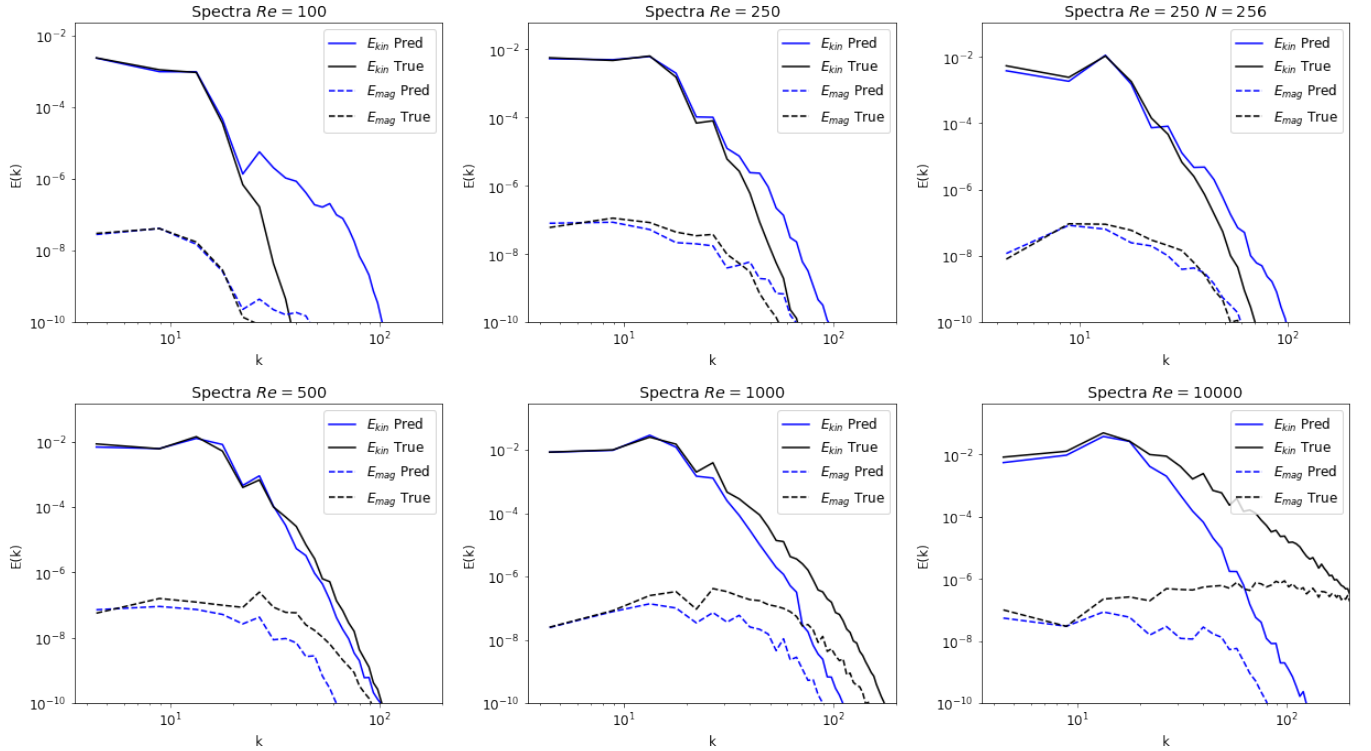


Figure 9 : Spectra The panels show the kinetic and magnetic spectra for each PINO model and simulation at time $t = 1$. We present the kinetic energy spectra as solid lines and the magnetic energy spectra as dashed lines. The ground truth simulations are illustrated in black while the PINO predictions are in blue. The top row presents from left to right the $Re = 100$, $Re = 250$, and $Re = 250$ with $N = 256^2$ grid points cases. The bottom row contains the $Re = 500$, $Re = 1,000$, and $Re = 10,000$ cases.